Hindawi
Advances in Civil Engineering
Volume 2020, Article ID 8825015, 13 pages
https://doi.org/10.1155/2020/8825015

*Research Article*

# Three-Dimensional Numerical Modeling and Roof Deformation Analysis of Yuanjue Cave Based on Point Cloud Data

**Zhigang Meng,[1,2,3] Manchao He,[1,2] Zhigang Tao,[1,2] Bin Li,[3] Gang Zhao,[4] and Mingru Xiao[3]**

[1]*State Key Laboratory for Geomechanics and Deep Underground Engineering, Beijing 100083, China*
[2]*School of Mechanics and Civil Engineering, China University of Mining and Technology, Beijing 100083, China*
[3]*Liaoning Non-Ferrous Geological Exploration and Research Institute Co., Ltd., Shenyang 110000, China*
[4]*Academy of Dazu Rock Carving, Chongqing, China*

Correspondence should be addressed to Zhigang Tao; taozhigang@263.net

Received 17 April 2020; Revised 1 October 2020; Accepted 24 November 2020; Published 2 December 2020

Academic Editor: Timothy O. Olawumi



Yuanjue Cave is the core exquisite cultural relic of the Dazu Stone Carvings World Cultural Heritage Site. For hundreds of years, with the continuous effect of natural forces and the erosion of various deterioration factors, the sidewall and roof rock mass of Yuanjue Cave were eroded, some parts of supporting rock mass were fragmented, and the boundary conditions of the rock mass have deteriorated, which have seriously endangered the Yuanjue Cave; once the roof collapses, the national treasure in the cave will be destroyed. In order to preevaluate the stability characteristics of the Yuanjue Cave rock mass and provide key parameters for the preventive protection of the Yuanjue Cave, this paper firstly established a refined database of key parameters of Yuanjue Cave and adjacent areas (geometry, geology, physical properties) based on three-dimensional laser point cloud scanning, a fine survey of adjacent areas, engineering geophysical prospecting, and indoor multifactor coupling tests. Then, based on FLAC3D finite difference numerical simulation technology, an accurate three-dimensional numerical calculation model of Yuanjue Cave was constructed. Finally, the model was used to analyze the roof stability of Yuanjue Cavern, revealing the deformation laws of the Yuanjue Cave roof under static load conditions, and the numerical calculation results were compared with the on-site measured results, verifying the feasibility of the high-precision modeling method, and the reliability of the numerical calculation results provided a reference for the preventive protection of the cultural relics of the cave temple.

## 1. Introduction

Most of the stone carvings of the cave temple are attached to the mountain. Cultural relics are directly carved on the cliff wall and connected with the mountain. Stone materials are the main material carriers of the cave temple cultural relics, which can be used as the artistic carrier of carving and painting and also as the carrier of the cave temple structures and buildings. The historical value and artistic value of cultural relics reside in the stone material carrier. Due to factors such as the diversity of material carriers, the complexity of the environment, and the changes in society, the preservation of the cultural relics of the cave temple has also been threatened to varying degrees [1].

In addition to the common problems of stone cultural relics such as sun and rain, mold growth, and surface weathering, the cultural relics of cave temples also face natural hazards such as cliff cracks, mountain collapse, water penetration, and tree rhizome splitting [2–6]. According to the results caused by the pathogenic factors, it can be divided into two categories: "stability of the surrounding rock of the grotto" and "repair and protection of the stone carvings" [7].

The issue of stability is the basis of the preventive protection of grotto cultural relics and determines the continuation of the value of grotto cultural relics and the inheritance of culture [8, 9]. There are a large number of grottoes and cliff sculptures in the Sichuan–Chongqing area of China. The most influential one is the Dazu Rock Carvings in Chongqing. Located in the northwest of Chongqing, Dazu Rock Carvings were excavated in the Tang Dynasty and flourished in the Song Dynasty. There are more than 50,000 statues and 100,000 inscriptions. They were included in the

"World Natural and Cultural Heritage List" in 1999. Yuanjue Cave is the core cultural relic of Dazu Rock Carvings, the internal sculpture of Yuanjue Cave is shown in Figure 1. It has a status and function that cannot be ignored in the history of Chinese grotto construction, carving art, and religious culture [10, 11].

Yuanjue Cave is located in a typical red sandstone environment in the Sichuan Basin, which is reddish-brown due to rich oxides. This kind of stone is delicate and low in strength and is widely used for carving. The Sichuan Basin is wet and rainy, and the red sandstone has strong water absorption, which is easy to breed various biological and physical diseases. For thousands of years, under the action of long-term natural forces and human factors, a series of stability problems have appeared on the roof of Yuanjue Cave: serious denudation of sidewall rock mass, fracture of supporting rock mass, deterioration of rock mass boundary conditions, and other serious threats to the Yuanjue Cave. The security of the cave is an objective phenomenon and has accelerated in recent years. Once the roof collapses, the national treasure in the cave will be destroyed. Therefore, the stability evaluation of Yuanjue Cave is urgently needed.

As an important rock mass stability evaluation method, numerical simulation technology has been widely used in mining engineering, water conservancy and hydropower engineering, and geotechnical engineering and has successfully solved many major engineering problems. This article uses FLAC3D software to evaluate the stability of Yuanjue Cave, and high-precision modeling is the basis of simulation evaluation. 3D geotechnical analysis software usually has disadvantages such as heavy workload and difficulty in depicting the structure of geological bodies, especially in complex processing. In the case of geological bodies, a lot of time is spent on preliminary modeling, which hinders its development and application in related fields [12–16].

3D laser scanning technology can realize the fine data collection of complex 3D geological bodies and assist in the rapid construction of numerical models. As an emerging surveying and mapping method, 3D laser scanning technology has shown strong technical advantages in many engineering applications and obtained a large number of research results [17–23]. For example, Dong et al. [24] believed that the emergence of 3D laser scanning technology is another technological revolution in the field of surveying and mapping after GPS technology; Chu et al. [25] systematically analyzed the technical advantages of 3D laser scanning technology in landslide, collapse investigation and monitoring, and limitations. Chen et al. [26] introduced the principle of the 3D laser scanning system, the causes of errors, and the data processing methods in foundation pit monitoring and discussed the application of this technology in foundation pit deformation monitoring. Wang et al. [27] proposed an earth-rock dam deformation monitoring method based on 3D laser scanning technology. Ge et al. [28] used 3D laser scanning technology to obtain point cloud data of rock mass outcrops. You et al. [29] based on 3D laser scanning technology used the dolomite structural plane of the reservoir in Guizhou Province as the research object, and the anisotropy of the fractal dimension of the structural plane is studied. Shi et al. [30] took Yungang No. 11 Grotto as the research object and used 3D laser scanning technology to quickly obtain point cloud data on the surface of the grotto and constructed the FLAC$^{3D}$ numerical calculation model of the grotto. Liu et al. [31] used 3D laser scanning technology to obtain rock mass high-precision point cloud data on the surface and the information of the rock mass fracture network. Liu et al. [32] used the 3D laser scanning technology of the empty area to complete the stability calculation of the underground empty area of the SAN Daochuang Open-Pit Mine. In short, three-dimensional laser scanning technology has been applied in engineering survey, surveying and mapping, deformation monitoring, rock mass structure surface statistics, dangerous rock mass survey, and so forth. It is in the rapid development stage, but the application of this technology is relatively shallow, and in the field of cultural relics protection is still little research.

In view of this, based on the results of the preliminary protection of the roof of Yuanjue cave, the author first adopted three-dimensional laser point cloud scanning, refined survey of adjacent areas, engineering geophysical exploration, and indoor multifactor coupling experiments, and other methods to obtain a refined database of key parameters of Yuanjue cave and adjacent areas; then, based on FLAC3D finite difference numerical simulation technology, an accurate three-dimensional numerical calculation model of Yuanjue cave was constructed; finally, the model was used to analyze the deformation law of roof rock mass in Yuanjue cave and provide a reference for the preventive protection of the cave temple cultural relics.

## 2. Spatial Characteristics and Roof Support Conditions of Yuanjue Cave

*2.1. Geometrical Space Characteristics of Yuanjue Cave.* According to the investigation, the orientation of the grottoes in Yuanjue Cave is NE∠44°, and the shape of the internal space is nearly regular hexahedron. The entrance tunnel is about 6.5 m long, the maximum height in the cave is 6.02 m, the width is 9.55 m, and the depth is 12.13 m (Figure 2). In order to further reveal the variation law of the space inside the Yuanjue Cave and the thickness of the roof rock mass, profile geological sketch maps are made along the direction and transverse direction of the Yuanjue Cave to analyze the geometric dimension characteristics of the inside and roof of the cave.

The structural characteristics of the current roof thickness of Yuanjue Cave are as follows:

(1) The surface layer of Yuanjue Cave is covered with a concrete protective layer, and the transparent hole extends to the wall. The rock at the light-transmission hole extends about 1 m outside the body, and the stress conforms to the stress characteristics of the cantilever beam.

(2) The wall roof thickness is 1.7 m and span 3.55 m. In the vertical section direction of A-A, the thickness of the top plate gradually thickens from the front

Figure 1: Internal structural features of Yuanjue Cave.

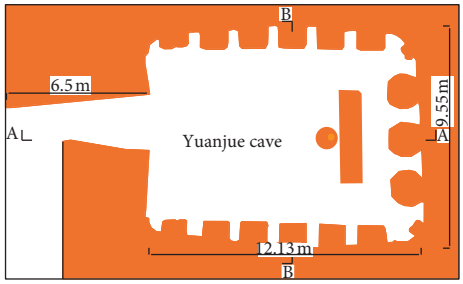


Figure 2: Structure characteristics of Yuanjue Cave in top view.

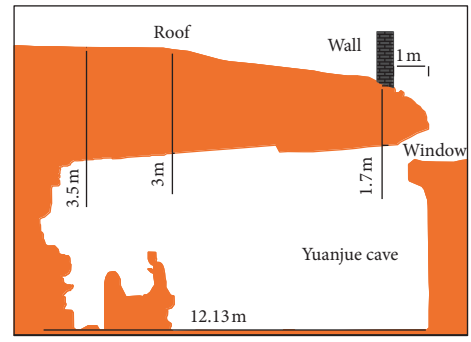


Figure 3: Structure characteristics of A-A section.

light-passing hole to the back chamber, reaching about 2.34 m thick at the middle top plate step (Figure 3).

(3) The thickness of the roof near the rear chamber is about 2.6–3.37 m, and the span is 9.04 mm. In the cross-sectional direction of B-B, the thickness of the top plate is not much different; generally, the difference is 0.1 m, and the maximum difference is about 0.3 m (Figure 4).

*2.2. Roof Support Conditions of Yuanjue Cave.* The roof rock mass of Yuanjue Cave was hollowed out at the lower part during the excavation of the cave. Due to J10 fissure cutting and water flow erosion on the east side, the support area on the east side will not be able to support the upper rock mass as the cave is excavated. The ancients skillfully solved this problem by filling the rock with strips. The same design also appeared on the west side of the light hole. With the gradual deepening of the investigation work, through the investigation of the supporting situation of the roof and the preservation status of the supporting body, it is found that the boundary length of the roof supported by the original rock in Yuanjue Cave is less than half of the whole boundary, as shown in Figure 5. On the one hand, the stone boundary can play a supporting role in the early stage of support and protect the long-term stability of Yuanjue Cave. On the other hand, due to the restriction of ancient scientific and technological level, the strip stone after construction is mainly in point contact or line contact with the roof. With the long-term deterioration of the strip stone over a span of hundreds of years by the deterioration factor, cracks develop at the filling strip stone on the east side of the light-transmitting hole, with local fragmentation damage, and the failure mode is mainly compression shear damage.

## 3. Geological and Lithological Characteristics of Yuanjue Cave

Yuanjue Cave is located on the cliff near the vertical face of the south cliff of the gulch in Giant Buddha Bay. The gulch runs near EW direction and is formed by erosion from east to west. The overall shape is "U", with a length of about 340 m and a width of about 90 m. The bottom elevation of the valley is about 462–473 m *m*. The height of the cliff is generally greater than 6 m.

The surrounding rock strata of Yuanjue Cave are all typical red bed sandstones in Sichuan Basin, which belong to the fluvial and lacustrine sedimentary environment. The strata are mainly composed of horizontal fine-grained sandstones and mudstone interbedded with thin-layer sandstone layers containing more flaky mica locally. The lithology of the strata changes strongly, and the interbedding of various sandstones and sandstones and mudstones is prominent. The lithology distribution of the south cliff where Yuanjue Cave is located and the relative relationship between Yuanjue Cave and cliff are shown in Figure 6. The changeable sedimentary environment leads to the complex and changeable nature of lithofacies and rock strata and forms a unique natural geographical landscape. The rock

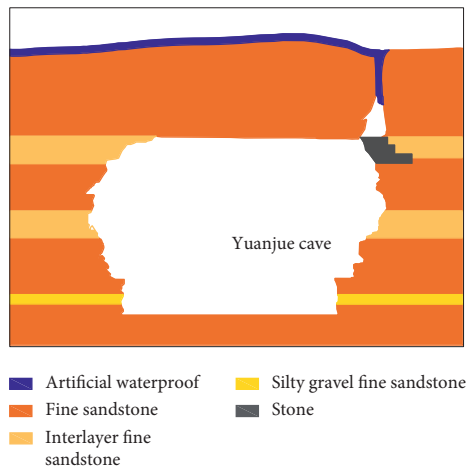


Figure 4: Structure characteristics of B-B section.

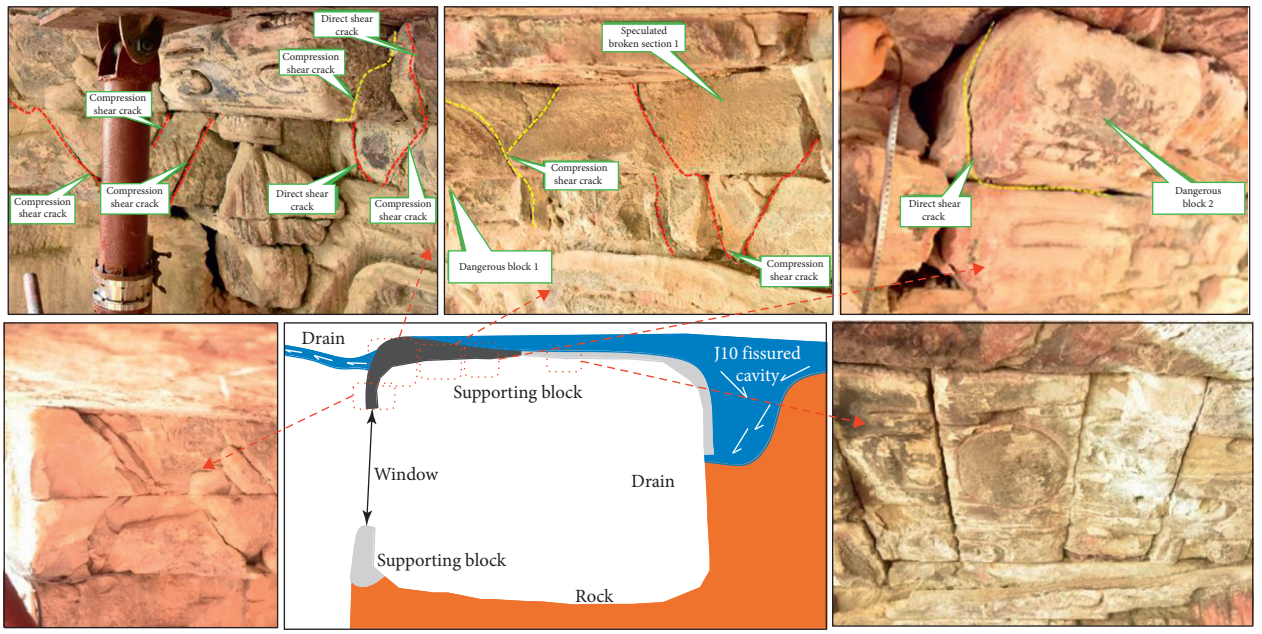


Figure 5: Breakage of supporting strips.

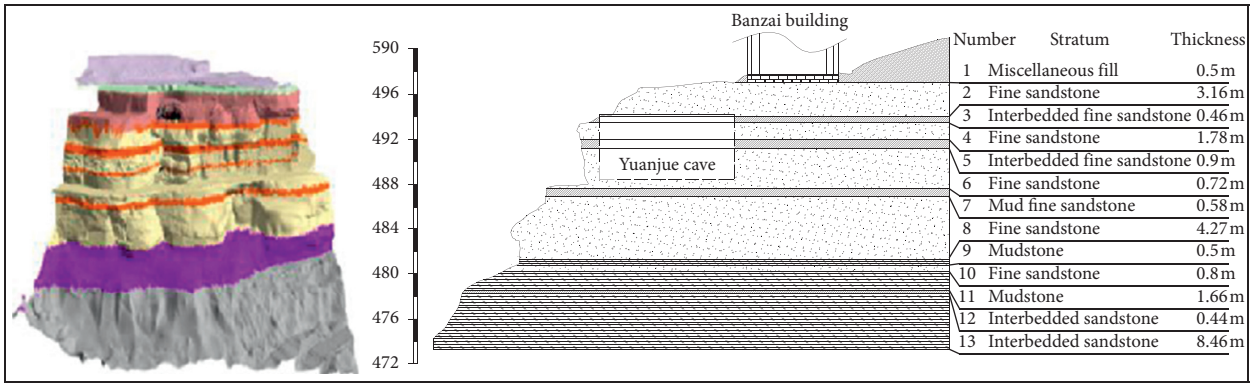


Figure 6: Lithological distribution of the south cliff of Giant Buddha Bay.

strata with better lithology and strong weathering resistance form a relatively prominent canopy structure, while the rock strata with weak nature shrink relatively under the action of weathering force. The statues carved on it can be protected by its upper canopy structure, avoiding direct wind and rain erosion, thus becoming a good statue cliff (Figure 7).

According to the investigation, 13 fissures are developed in the surrounding rock mass around Yuanjue Cave, and each fissure is dislocated or pinches out at the weak rock stratum, resulting in different appearance of the main fissures developed in the adjacent strata. Among them, the main fissures that directly cut the surrounding rock body of Yuanjue Cave are J-01, J-07, J-10, L05, L06, and L08. Among them, L6 fissures are only developed in the roof layer, and J01, J07, J10, L05, and L08 fissures are exposed in the image layer and the bottom rock body of Yuanjue Cave. The distribution characteristics of the main fissures in different layers are shown in Figure 8.

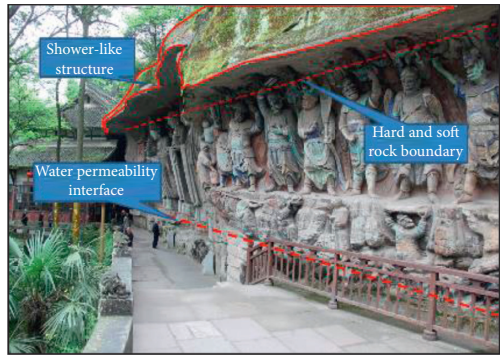


Figure 7: Topographic characteristics of statue layers.

## 4. Construction of Three-Dimensional Numerical Model of Yuanjue Cave Based on Point Cloud Data

*4.1. High-Precision Solid Modeling.* Data acquisition is carried out by combining three-dimensional scanning and traditional measurement technology. The instrument adopts Soja NET05 0.5″ "total station and its matching prism (angle measurement accuracy is 0.5"; ranging accuracy is ± s(1 mm + 1 ppm)), FARO Focus3D X 330 HDR three-dimensional laser scanner, FARO SCENE software, and Geomagic software. According to the spatial characteristics of the research object, when setting up a 3D scanner for three-dimensional scanning, a special target for 3d scanner will be set up around it. The coordinate values of the target will be measured by a total station to introduce the three-dimensional scanning data into the geodetic coordinate control network of the project. A total of 55 stations were scanned.

This simulation is based on image point cloud data, with a holographic image as the foreground representation and point cloud as the background support. The holographic image and point cloud are closely registered and fused to complete the surface model modeling, and appropriate grid division is carried out on this basis. Due to the huge amount of data and considering the accuracy impact degree of simulation analysis, this project reduces the accuracy of the model surface (Buddha statue, text, sculpture, etc.) to about 10 cm, and the contact accuracy of blocks is within 3 mm.

The roof model of Yuanjue Cave established in this paper is mainly to simulate the structural interaction between roof rock mass and lower supporting block, so its simulation scope should include independent roof block, lower supporting rock mass and strip rock structure. The fracture that can cover the above blocks is taken as the boundary, and the model boundary is parallel to the axial direction of the cave body. The specific model size is as follows: the east side is bounded by 5 m east of J10 fracture, the south side is bounded by 5 m south of the dew point of L6 fracture, the west side is bounded by the dew point of L6 cliff, and the north side is bounded by cliff. The length of the model along the longitudinal axis of Yuanjue Cave is 20 m, the width of the vertical longitudinal axis is 19 m, and the height of the model is 11 m.

*4.2. Geomechanical Parameters.* The lithology parameters of this simulation are determined by taking rock samples from on-site drilling and indoor rock tests, and by combining the parameter differences between rock blocks and rock masses, the execution of the rock mechanics tests are carried out according to the standard for test methods of engineering rock mass (GB/T 50266-2013). Specific formation parameters are presented in Table 1.

*4.3. Application and Calculation of Additional Loads.* The cave body of Yuanjue Cave is excavated in the cliff rock body. The roof rock body is connected with the foundation of the banzai building. The relative position of the support column of the banzai building and Yuanjue Cave is shown in Figure 9. Long live building is an octagonal wooden tower structure, with a height of 21.2 m and a width of 3.6 m at the bottom. It is located directly behind the upper part of Yuanjue Cave and spans the J10 fissure. The eaves columns in the east and north of the long live building are located above the J10 fissure cavity, the northeast eaves column is located on the east side of J10 fissure, and the other 5 eaves columns are located on the west side of J10 fissure. Only one eave column facing southeast is located above the roof of Yuanjue Cave, and the center of the column is 0.7 m away from the rock face behind the cave. According to the relevant load value standard of ancient buildings, the load of banzai building is counted. The relevant load values are shown in Table 2.

According to the calculated load and distribution characteristics in this table, the load of the banzai building is mainly distributed on the inner ring columns, and at the same time, the load is converted into normal (vertical) pressure value (200 kPa) and applied according to the cross-sectional area of the columns (Figure 10).

*4.4. Analysis of Cracks and Boundary Conditions.* Based on the fine detection results, FLAC3D built-in interface unit is

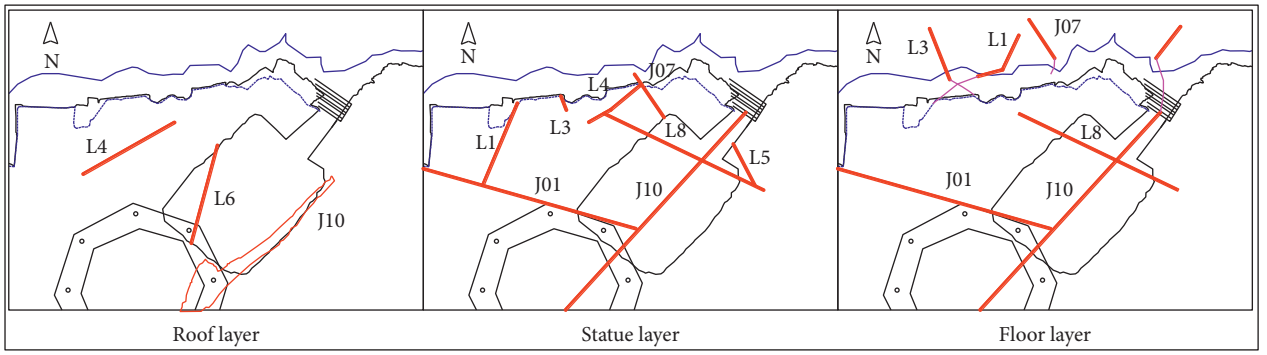


Figure 8: Distribution characteristics of main cracks in Yuanjue Cave.

Table 1: Parameters of formation lithology.

| Number | Stratum | Depth (m) | Elastic modulus (Pa) | Poisson's ratio | Cohesive strength (Pa) | Internal friction angle (°) | Density (kg/m$^3$g) |
|---|---|---|---|---|---|---|---|
| 1 | Miscellaneous fill | 25.2–70 | $1.00E+09$ | 0.41 | $2.50E+04$ | 18 | 1660 |
| 2 | Fine sandstone | 22.3–25.2 | $2.76E+10$ | 0.17 | $1.35E+06$ | 33 | 2230 |
| 3 | Interbedded fine sandstone | 21.8–22.33 | $1.38E+10$ | 0.25 | $9.00E+05$ | 34 | 2150 |
| 4 | Fine sandstone | 20.1–21.8 | $2.50E+10$ | 0.18 | $1.50E+06$ | 32 | 2200 |
| 5 | Interbedded fine sandstone | 19.23–20.1 | $1.38E+10$ | 0.25 | $9.00E+05$ | 33 | 2040 |
| 6 | Fine sandstone | 15.67–19.23 | $2.50E+10$ | 0.18 | $1.50E+06$ | 35 | 2240 |
| 6-1 | Mud fine sandstone | 15.38–15.67 | $1.00E+10$ | 0.3 | $6.00E+05$ | 33 | 2160 |
| 7 | Mud fine sandstone | 14.74–15.38 | $1.00E+10$ | 0.3 | $6.00E+05$ | 32 | 2230 |
| 8 | Fine sandstone | 10.72–14.74 | $2.50E+10$ | 0.18 | $1.50E+06$ | 34 | 2270 |
| 8-1 | Fine sandstone | 7.82–10.72 | $2.50E+10$ | 0.18 | $1.50E+06$ | 36 | 2210 |
| 9 | Mudstone | 7.34–7.82 | $6.00E+09$ | 0.35 | $8.00E+05$ | 37 | 2360 |
| 10 | Fine sandstone | 6.61–7.34 | $2.50E+10$ | 0.18 | $1.50E+06$ | 38 | 2160 |
| 11 | Mudstone | 5.35–6.61 | $6.00E+09$ | 0.35 | $8.00E+05$ | 39 | 2310 |
| 12 | Fine sandstone | 4.33–5.35 | $2.50E+10$ | 0.18 | $1.50E+06$ | 42 | 2350 |
| 13 | Mudstone | −3.2–4.33 | $6.00E+09$ | 0.35 | $8.00E+05$ | 32 | 2260 |

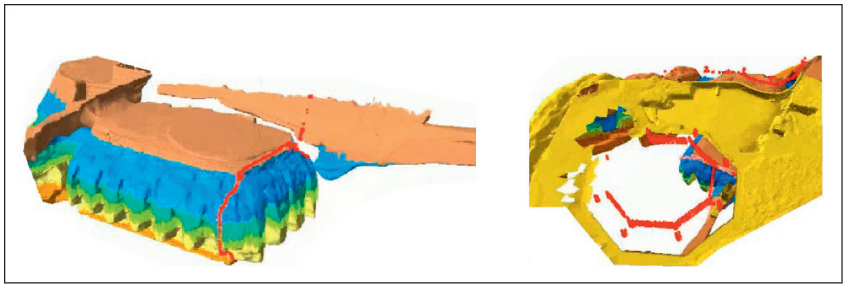

Figure 9: Spatial relationship between Banzai building, Yuanjue Cave, and J10 fissure.

Table 2: Banzai building load statistics.

| Number | Projects | Value | Unit | Quantity | Calculated load value/$t$ |
|---|---|---|---|---|---|
| 1 | Level live load | 3.6 | kN/m$^2$ | 112.37 | 40.453 |
| 2 | Constant load (converted into wood) | 550 | kg/m$^3$ | 78.66 | 43.262 |
| 3 | Glazed tile (including grey quilt) | 174.3 | kg/m$^2$ | 278.872 | 48.607 |
| 4 | Coloured glaze ridges | 94.5 | kg/m | 96.576 | 9.126 |
| 5 | Total | — | — | — | 141.4 |
| 6 | Average column load per group | — | — | — | 17.7 |

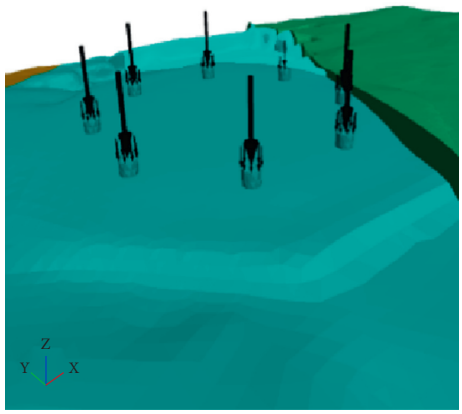


Figure 10: Load application of Banzai building.

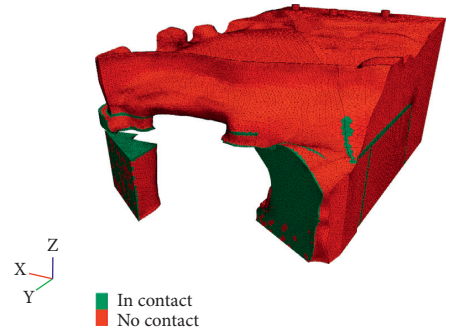


Figure 11: Contact of cracks in the partial model of Yuanjue Cave.

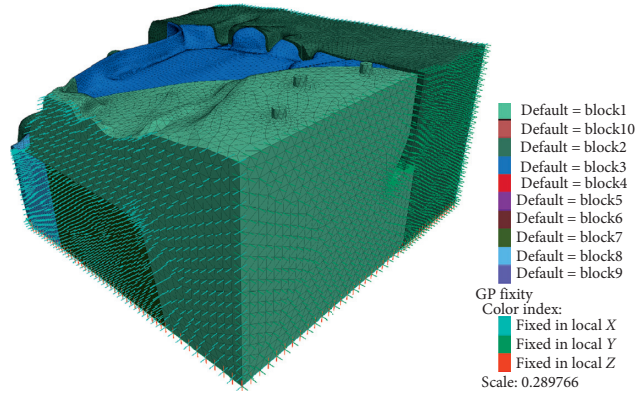


Figure 12: Boundary constraints of roof model of Yuanjue Cave.

used to simulate the three-dimensional structural characteristics of the fracture interface. Due to the complex spatial form of fractures in Yuanjue Cave, it is extremely difficult to model the fractures through a single fracture. Therefore, a modeling method is proposed in which the local model is wrapped by the interface elements on the surface of key blocks. After the local block is wrapped by the contact surface, the contact conduction between the local block and the surrounding block can be completed by the contact surface unit at the contact position. Figure 11 shows the interface contact situation. The model is manually cut, and there are 4 manually cut boundaries, of which the bottom boundary fixes all nodes $X$, $Y$, and $Z$ in the plane, and both sides and rear of the model adopt horizontal fixed boundaries (Figure 12). After the constraint boundary of the model is established, the linear elastic model is firstly adopted to carry out self-balancing under the gravity field condition. Then, the calculation is carried out in the elastoplastic phase of the Moore–Coulomb model, and the maximum unbalance force $F_m < 1e^{-5}$ N is taken as the end mark of the calculation. Finally, the stress characteristics of the roof and its lower supporting bars of Yuanjue Cave, the stability risk of the roof of Yuanjue Cave, and the strain characteristics of the roof plate are revealed.

## 5. Analysis of Roof Deformation Law of Yuanjue Cave

### 5.1. Analysis on Stress Field and Its Evolution Law of Roof in Yuanjue Cave

*5.1.1. Stress Distribution Characteristics of Roof and Supporting Blocks in Yuanjue Cave.* Firstly, the top plate of Yuanjue Cave and the strip supporting the top plate are taken as the main analysis objects. Figure 13(a) shows the distribution characteristics of the horizontal stress field of Yuanjue Cave. Warm color represents tensile stress and cold color represents compressive stress in the nephogram. The figure shows that there is a horizontal compressive stress concentration area (0.5–1 MPa) in the middle above the light hole on the upper surface of the top plate of Yuanjue Cave, with a depth of about 60 cm. Corresponding to the lower part, there is a tensile stress concentration area (0.25–0.5 MPa) with a depth of 40 cm. This figure shows that the bending moment of the top plate of Yuanjue Cave is mainly concentrated in the middle position of the front part (window side), with a horizontal direction.

Figure 13(b) shows the stress situation of the support block at the lower part of Yuanjue Cave. The distribution laws of different stress types are roughly the same, showing that in the support areas on both sides of the window, the pressure concentration degree in the support area on the east side is greater than that on the west side, the filling bar stone is used as the main stress body on the east side, and the concentration pressure in the front section of the bar stone on the east side is greater than that in the rear section.

Figure 13(c) shows the stress and deformation distribution of the fillets in the lower part of the roof of Yuanjue Cave. In order to highlight the segmented and segmented deformation characteristics of the fillets, only the deformation nephogram of the fillets is called out. The deformation law of the fillets is similar to the stress concentration of the fillets. The deformation amount of the fillets on the east side of the overall window is larger than that on the west side, and the deformation amount in the front part of the fillets on the east side is larger than that in the back part of the fillets. However, the deformation amount of the fillet in some parts is different from the stress distribution, for example, the deformation amount of the fillets in the inner

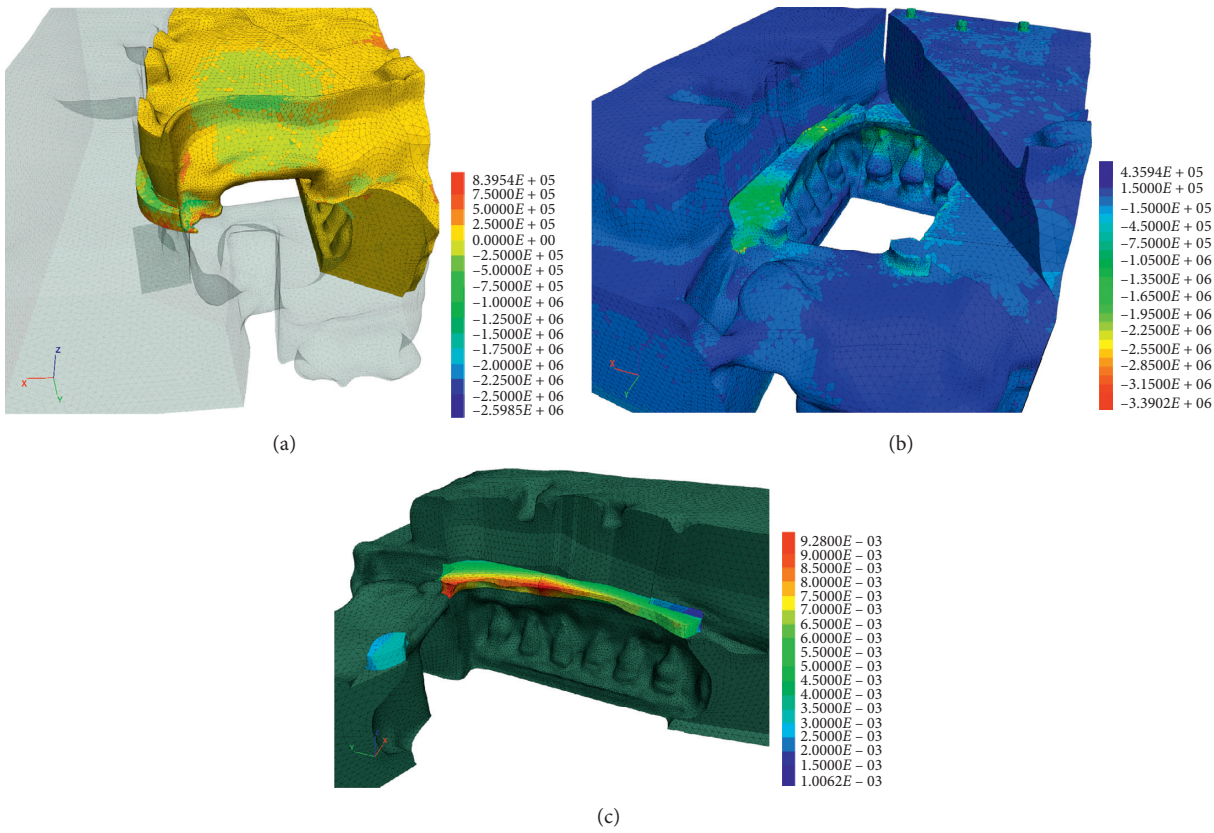


Figure 13: Stress nephogram of local model of Yuanjue Cave. (a) Horizontal stress field of roof, (b) maximum principal stress field of the supporting block, and (c) deformation characteristics of supporting blocks.

edge of the east side is larger and more concentrated in the front part.

*5.1.2. Characteristics of Roof Stress Traces in Yuanjue Cave.* By taking the main stress trace inside the roof of Yuanjue Cave as the analysis object, only the independent roof plate body of Yuanjue Cave is called out, and the stress characteristics inside the roof are given by the magnitude and spatial deflection characteristics of the three-dimensional main stress (maximum main stress, intermediate main stress, and minimum main stress). Since the principal stresses are all compressive stresses, the calculated value in the software is negative, and the larger the absolute value, the smaller the displayed value; that is, the displayed minimum value is the actual maximum value (absolute value). Figure 14(a) is a three-dimensional perspective view of the stress trace inside the top plate (left rear end view of the model). In this view, the trace of the maximum principal stress (white short line) at the support positions at both ends of the top plate tends to be vertical and gradually deflects toward the horizontal direction after entering the top plate body upward, and the maximum principal stress dominance is distributed near the upper surface, while the trace concentration area of the intermediate principal stress (purple line) is mainly distributed near the lower surface of the top plate body.

Figure 14(b) is a cut trace of the upper half of the roof, showing the horizontal deflection characteristics of the upper main stress trace of the roof. In order to show the trace more clearly, adjust the maximum principal stress trace from white to yellow according to the picture background. The deflection track of the maximum principal stress trace presents Y-type diffusion and echoes with each end of the roof triangle, forming a relatively regular stress form near the upper surface of the roof rock mass. On the other hand, the concentration of the stone filling side (east side) on the east side of the window is significantly greater than that on the west side (L6 cutting side). The maximum principal stress starts at the lower three supporting areas, and the maximum principal stress is transferred from the supporting areas to the upper half of the roof and finally collected near the centroid.

Figure 14(c) shows that the main stress concentrated in the lower part of the top plate is mainly the middle main stress by intercepting the trace of the lower part of the top plate. The trace flow pattern corresponds to the maximum main stress pattern in the upper part and is also triangular flow, gradually converging from three supporting points to the position of the geometric center of the inner surface.

*5.2. Analysis of Roof Displacement Field and Its Evolution Law in Yuanjue Cave.* The model calculation is a quasistatic

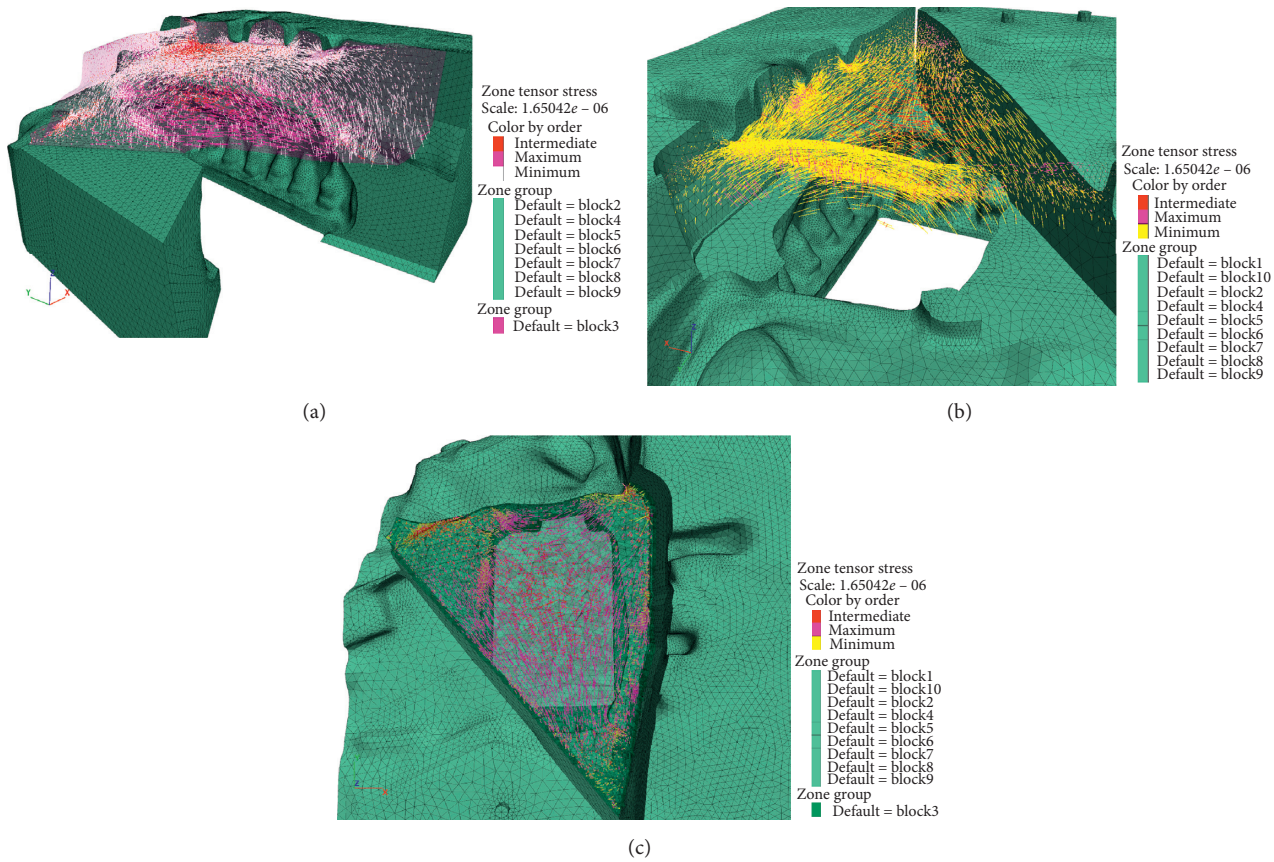


Figure 14: Stress trace diagram of the local model of Yuanjue Cave. (a) Overall stress trace of the roof, (b) stress trace in the top half of roof, and (c) stress trace in the lower half of the roof.

calculation. The model changes from elastic calculation process to elastic-plastic calculation process, which is the deformation process of the roof. Due to the complexity of roof lithologic parameters and deformation influencing factors of Yuanjue Cave, numerical simulation methods have not yet been able to accurately simulate the evolution process of the cave for more than 800 years. The obtained simulated deformation data are only used to study its deformation mechanism and serve the rescue protection work of Yuanjue Cave. The roof displacement characteristics of Yuanjue Cave are shown in Figure 15.

(1) Figures 15(a) and 15(b) show that the main deformation parts of the model are concentrated in the roof and its lower supporting strips on the east side of Yuanjue Cave, and the more the strip filling area approaches the front window, the greater the deformation. Generally speaking, the east side is larger than the west side, and the northeast corner has the largest deformation.

(2) Figure 15(c) shows the deformation nephogram of L6 cutoff section, which shows that the deformation on this section forms a uniform transition section with "upper left corner-lower right corner" as the connecting line. It shows that the roof deformation of Yuanjue Cave gradually increases from the northwest corner to the east, with uniform gradient, which accords with the block deflection characteristics. It is judged that the roof deformation is mainly deflection deformation, and the deflection axis is located in the L6 fracture cutting section.

*5.3. Analysis on Evolution Law of Displacement Monitoring Points of Roof in Model.* According to the roof shape and thickness distribution characteristics of Yuanjue Cave, a total of 78 displacement monitoring points were designed this time. Among them, a total of 4 rows of 11 displacement monitoring positions are arranged from the window position to the inside of the plane. Each monitoring position is designed with 7–10 displacement monitoring points according to the change of the roof thickness; the vertical monitoring points are arranged at a distance of 30–35 cm. The change characteristics of settlement displacement are shown in Figure 16.

(1) Figure 16(a) shows the settlement of three monitoring points 1.5 m away from the window, showing that the maximum settlement is 8.04 mm and the minimum is 4.09 mm. The displacement of the monitoring points on the east side of the roof (the side where the strips are filled) is significantly larger than the west. The vertical monitoring points in the roof layer at the same location have a maximum

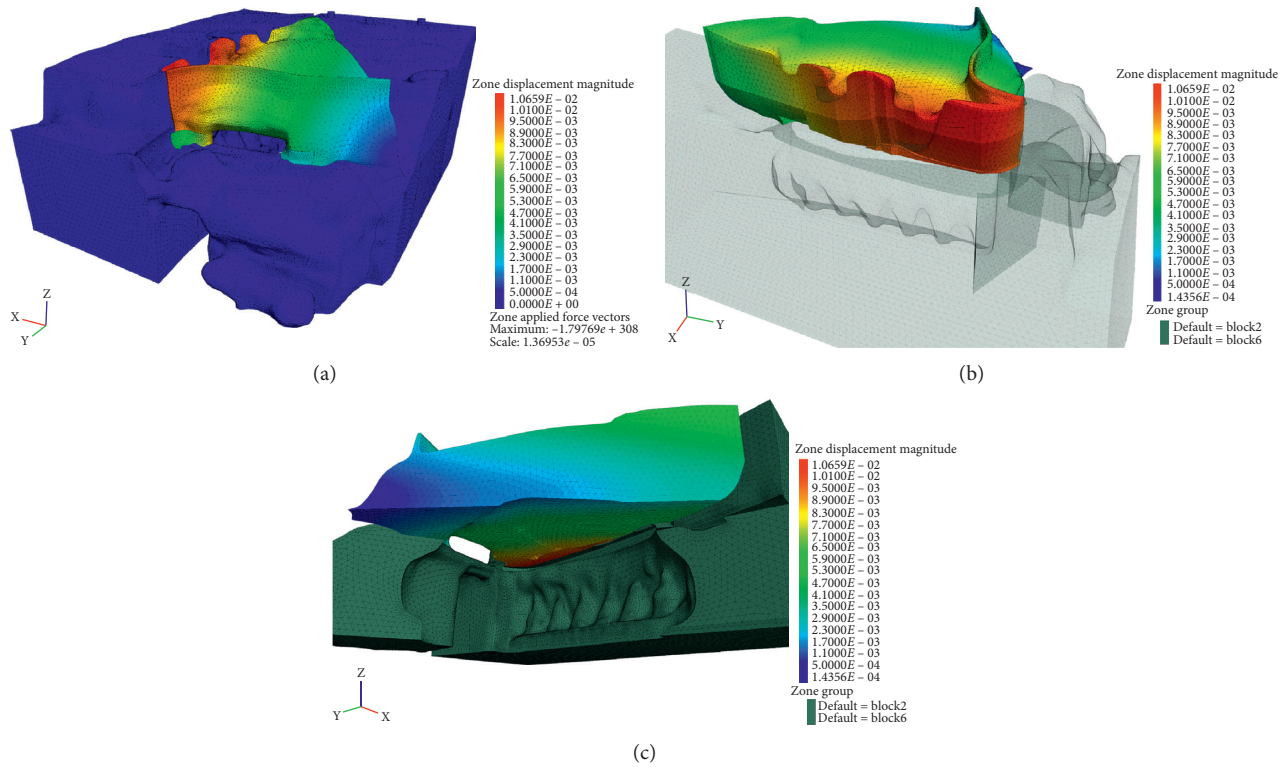


Figure 15: Displacement nephogram of Yuanjue Cave local model. (a) Nephogram of total displacement, (b) displacement of roof (perspective 1), and (c) displacement of roof (perspective 2).

settlement difference of 0.01 mm, and the vertical point monitoring curves at each location basically overlap.

(2) Figure 16(b) shows the settlement of three monitoring points 3.5 m away from the window, showing that the maximum settlement is 8.04 mm and the minimum is 2.84 mm. The overall rule is that the settlement on the east side is greater than that on the west side, and the vertical monitoring point at the same location. The settlement difference is small, the maximum difference is 0.01 mm.

(3) Figure 16(c) shows the settlement of two monitoring points 7 m away from the window. It shows that the maximum settlement is 7.72 mm, the minimum settlement is 4.96 mm, and the maximum settlement difference between the vertical monitoring points at the same location is 0.01 mm.

(4) Figure 16(d) shows the settlement of three monitoring points 11 m away from the window, showing that the maximum settlement is 5.04 mm, the minimum settlement is 2.07 mm, and the vertical monitoring point settlement at the same location has a maximum difference of 0.04 mm, which is significantly larger than other locations, which shows that due to the poor stress conditions at this location, combined with the layered sedimentary characteristics of the roof rock mass, it is judged that there is a risk of layer separation. Field observations revealed that the erosion of the back section of the roof was significantly greater than that of the front section, and the maximum amount of erosion differed by 250 mm, which also confirmed the law derived from the monitoring point data.

According to the roof shape and thickness distribution characteristics of Yuanjue Cave, 91 displacement monitoring points are designed. Among them, 4 rows of 11 displacement monitoring positions are arranged from the window position to the inside of the plane, and 7–10 displacement monitoring points are designed for each monitoring position according to the thickness change of the roof. The distance between vertical monitoring points is 30–35 cm. The displacement variation characteristics of monitoring points are shown in Figure 16.

(1) The curve in Figure 16(a) shows that the displacement on the east side of the roof of Yuanjue Cave (the side filled with stone) is obviously larger than that on the west side, and the direction of the front window is obviously larger than that on the back side.

(2) The displacement curves shown in Figure 16(b) are completely coincident, and there is no possibility of delamination along the vertical direction.

(3) Figure 16(c) shows that the displacement curves are not completely coincident, and the maximum difference is 0.02 mm, which indicates that there is delamination risk in this part due to geometric shape and stress distribution, which is consistent with the

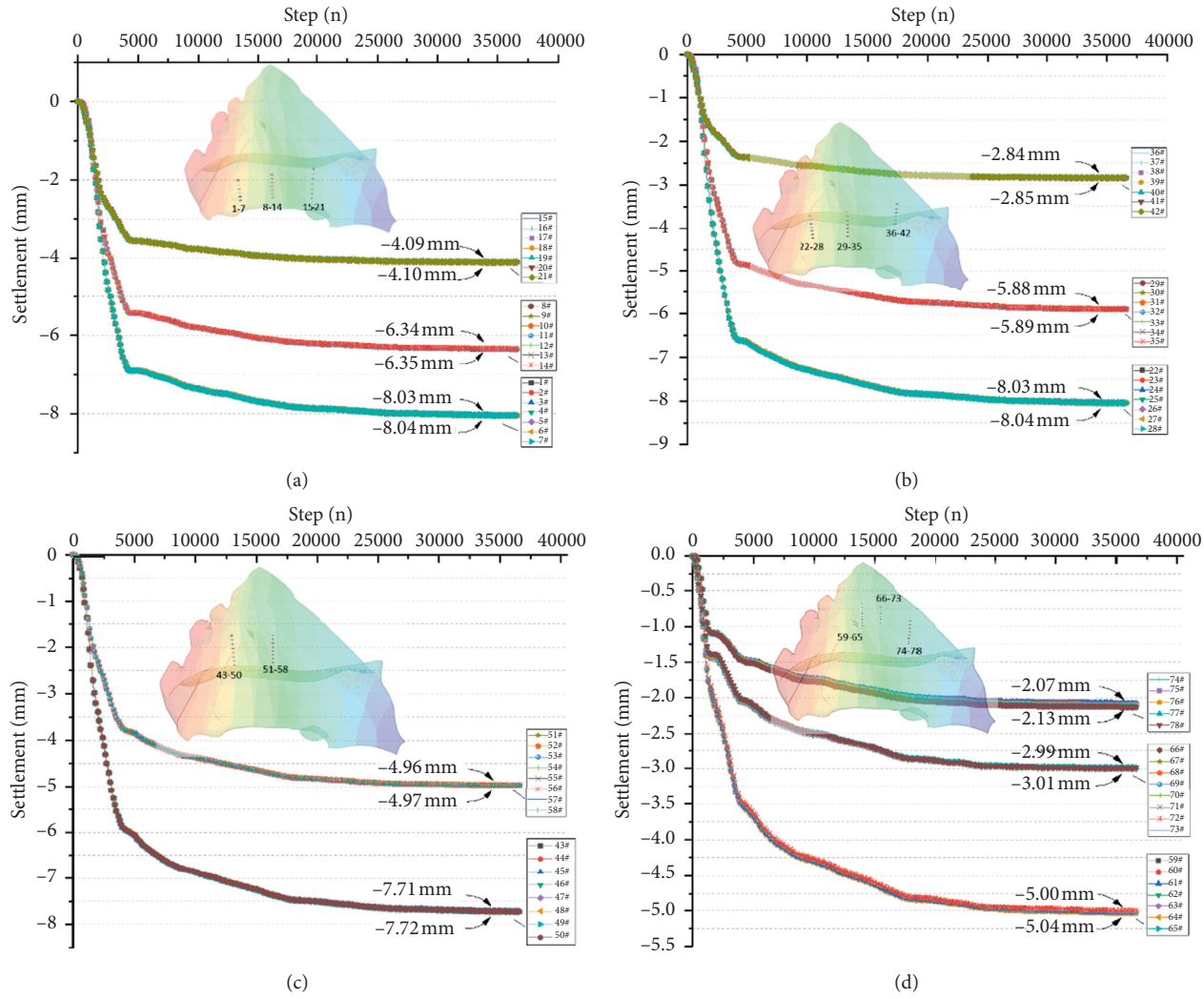


Figure 16: Monitoring curve of roof displacement monitoring points in Yuanjue Cave. (a) Displacement monitoring curve of measuring point (1–21#), (b) displacement monitoring curve of measuring point (22–42#), (c) sisplacement monitoring curve of measuring point (43–58#), and (d) displacement monitoring curve of measuring point (59–78#).

actual situation on site (the denudation depth of this part is the largest).

## 6. Conclusion

Based on the point cloud data method, the three-dimensional numerical model of Yuanjue cave is built, and the deformation of the roof is analyzed; some conclusions are drawn as follows:

(1) The roof volume of Yuanjue Cave is 256.03 $m^2$, the total weight is about 1360.8 t, the center of gravity is located in the center of plane space in Yuanjue Cave, the supporting triangle area on the west side of the window is 15.36 $m^2$, the supporting strip area on the west side of the window is 1.4 $m^2$, the supporting strip area on the east side is 8.2 $m^2$, and the supporting triangle area on the rear wall is 5.65 $m^2$.

(2) The average stress in the tensile zone on the lower surface of the roof of Yuanjue Cave is 0.8 Mpa, and the average stress in the compressive zone on the upper surface is 1.5 Mpa. The average compressive strength of the strips is 2.6 Mpa, and the maximum concentrated pressure of the strips is 3.5 Mpa, showing the basic rule that the stress of the strips on the east side of the window (the strip filling area) is greater than that on the west side of the window, and the stress of the strips on the east side is greater than that on the south side. The deformation of the strip rock is basically distributed in such a way that the inside of the cave is larger than the outside and the north section is larger than the south section.

(3) The deformation of the roof in Yuanjue Cave is larger in the east than in the west and northeast. The roof deformation of Yuanjue Cave gradually increases from the northwest corner to the east with a uniform

gradient, which accords with the characteristics of block migration.

(4) Vertical monitoring points are arranged along the thickness of the roof. Displacement data show that the displacement curves of the monitoring points at the same horizontal position in the southern section of the vertical boundary on the west side of the roof (at the back of the cavern) are not completely coincident with each other, with the maximum difference of 0.02 mm. Due to the geometric shape and stress distribution, there is a risk of delamination in the site, which is also consistent with the actual situation on site (the site has the largest denudation depth).

## Data Availability

The data used to support the findings of this study are included within the article.

## Conflicts of Interest

The authors declare that they have no conflicts of interest.

## Acknowledgments

This work was supported by Dazu District Science and Technology Commission Project Funding (no. DZKJ,2018ABB1011).

## References

[1] K. Huang, "Thoughts on the protection of stone cultural relics," *Chinese Cultural Heritage*, vol. 21, no. 4, pp. 4–12, 2018.

[2] D. Liu, Z. Gu, R. Liang et al., "Impacts of pore-throat system on fractal characterization of tight sandstones," *Geofluids*, vol. 2020, no. 9, pp. 1–17, Article ID 4941501, 2020.

[3] F. Q. Ren, C. Zhu, and M. C. He, "Moment tensor analysis of acoustic emissions for cracking mechanisms during schist strain burst," *Rock Mechanics and Rock Engineering*, vol. 53, no. 1, pp. 153–170, 2020.

[4] H. Y. Pan, D. W. Yin, N. Jiang, and Z. G. Xia, "Crack initiation behaviors of granite specimens containing crossing-double-flaws with different lengths under uniaxial loading," *Advances in Civil Engineering*, vol. 2020, p. 13, Article ID 8871335, 2020.

[5] C. Zhu, X. Xu, W. Liu et al., "Softening damage analysis of gypsum rock with water immersion time based on laboratory experiment," *IEEE Access*, vol. 7, pp. 125575–125585, 2019.

[6] J. T. Chen, J. H. Zhao, S. C. Zhang, Y. Zhang, F. Yang, and M. Li, "An experimental and analytical research on the evolution of mining cracks in deep floor rock mass," *Pure and Applied Geophysics*, vol. 17, 2020.

[7] J. Wang, *Research on Analysis and Evaluation System of Stability of Grotto Rock Structure*, China University of Geosciences Press, Beijing, China, 2013.

[8] S. She and L. Peng, "Some developments and challenging issues in rock engineering field in China," *Chinese Journal of Rock Mechanics and Engineering*, vol. 33, no. 3, pp. 433–457, 2014.

[9] L. Cheng-yu and H. Man-chao, "Study on the deformation failure mechanism and stability of ancient kings tomb:A case of national key cultural relic Gaogouli's Tai kings tomb," *Hydrogeology & Engineering Geology*, vol. 15, no. 5, pp. 25–28, 2007.

[10] Z. Guo, *Stability Analysis of Dense Caves and Risk Assessment of the Dangerous Rock Body at the Southern Area of Mogao Grottoes, Dunhuang*, Lanzhou University, Lanzhou, China, 2018.

[11] J. Wang and J. Chen, "An analysis of the status quo and development of the protection of Chinese cave temples," *Southeastern Culture*, vol. 28, no. 1, pp. 6–14, 2018.

[12] C. Zhu, Z. Yan, Y. Lin, F. Xiong, and Z. Tao, "Design and application of a monitoring system for a deep railway foundation pit project," *IEEE Access*, vol. 7, no. 1, pp. 107591–107601, 2019.

[13] C. X. Wang, B. T. Shen, J. T Chen et al., "Compression characteristics of filling gangue and simulation of mining with gangue backfilling: an experimental investigation," *Geomechanics and Engineering*, vol. 20, no. 6, pp. 485–495, 2020.

[14] G. Feng, Y. Kang, X. Wang, Y. Hu, and X. Li, "Investigation on the failure characteristics and fracture classification of shale under brazilian test conditions," *Rock Mechanics and Rock Engineering*, vol. 53, no. 7, pp. 3325–3340, 2020.

[15] J. Xu, A. Haque, W. Gong et al., "Experimental study on the bearing mechanisms of rock-socketed piles in soft rock based on micro X-ray CT analysis," *Rock Mechanics and Rock Engineering*, vol. 53, no. 8, pp. 3395–3416, 2020.

[16] C. Zhu, M. C. He, M. Karakus, X. B. Cui, and Z. G. Tao, "Investigating toppling failure mechanism of anti-dip layered slope due to excavation by physical modelling," *Rock Mechanics and Rock Engineering*, vol. 225, 2020.

[17] Q. Wang, B. Jiang, R. Pan et al., "Failure mechanism of surrounding rock with high stress and confined concrete support system," *International Journal of Rock Mechanics and Mining Sciences*, vol. 102, pp. 89–100, 2018.

[18] Q. Wang, Z. X. Xin, B. Jiang et al., "Comparative experimental study on mechanical mechanism of combined arches in large section tunnels," *Tunnelling and Underground Space Technology*, vol. 99, Article ID 103386, 2020.

[19] Q. Wang, Q. Qin, B. Jiang, H. C. Yu, R. Pan, and S. C. Li, "Study and engineering application on the bolt-grouting reinforcement effect in underground engineering with fractured surrounding rock," *Tunnelling and Underground Space Technology*, vol. 84, pp. 237–247, 2019.

[20] X. Wang, C. Liu, S. Chen, L. Chen, K. Li, and N. Liu, "Impact of coal sector's de-capacity policy on coal price," *Applied Energy*, vol. 265, Article ID 114802, 2020.

[21] Q. Wang, Z. Jiang, B. Jiang, H. Gao, Y. Huang, and P. Zhang, "Research on an automatic roadway formation method in deep mining areas by roof cutting with high-strength bolt-grouting," *International Journal of Rock Mechanics and Mining Sciences*, vol. 128, Article ID 104264, 2020.

[22] G. Feng, X. C. Wang, M. Wang, and Y. Kang, "Experimental investigation of thermal cycling effect on fracture characteristics of granite in a geothermal-energy reservoir," *Engineering Fracture Mechanics*, vol. 235, pp. 1–16, Article ID 107180, 2020.

[23] Q. Meng, H. Wang, M. Cai, W. Xu, X. Zhuang, and T. Rabczuk, "Three-dimensional mesoscale computational modeling of soil-rock mixtures with concave particles," *Engineering Geology*, vol. 277, Article ID 105802, 2020.

[24] X. Dong and R. Huang, "Application of 3d laser scanning technology to geologic survey of high and steep slope," *Chiese Journal of Rock Mechanics and Engineering*, vol. 188, no. S2, pp. 3629–3635, 2006.

[25] H. Chu, Y. Yin, F. Cao et al., "Research on deformation monitoring of large collapses and landslides based on 3D laser scanning technology," *Hydrogeology & Engineering Geology*, vol. 42, no. 3, pp. 128–134, 2015.

[26] Z. Chen, L. Chen, and J. Yang, "Application of three-dimensional laser scanning technique in deformation monitoring of excavations," *Chinese Journal of Geotechnical Engineering*, vol. 34, no. S1, pp. 557–559, 2012.

[27] J. Wang and C. Zhang, "Deformation monitoring of earth-rock dams based on three-dimensional laser scanning technology," *Chinese Journal of Geotechnical Engineering*, vol. 36, no. 12, pp. 2345–2350, 2014.

[28] Y. Ge, X. Ding, and H. Tang, "Intelligent identification and extraction of geometric properties of rock discontinuities based on terrestrial laser scanning," *Chiese Journal of Rock Mechanics and Engineering*, vol. 36, no. 12, pp. 3050–3061, 2017.

[29] Z. You, L. Wang, Y. Yang et al., "Anisotropic research on shear strength parameters of discontinuity based on three-dimensional laser scanning technology," *Chiese Journal of Rock Mechanics and Engineering*, vol. 33, no. S1, pp. 3003–3008, 2014.

[30] J. Shi, "Application of three-dimensional laser scanning technology in historic stone's numerical simulation," *Journal of Zhengzhou University of Light Industry (Natural Science)*, vol. 30, no. Z2, pp. 70–75, 2015.

[31] C. Liu, S. Zhang, L. Ding et al., "Identification of dangerous rock mass of high slope and study of anchoring method based on laser scanning," *Chiese Journal of Rock Mechanics and Engineering*, vol. 30, no. 11, pp. 2330–2337, 2011.

[32] K. Liu, X. Li, F. Gong et al., "Stability analysis of complicated cavity based on cals and coupled surpac-flac 3d technology," *Chiese Journal of Rock Mechanics and Engineering*, vol. 19, no. 9, pp. 1924–1931, 2008.